An application of one-sided Jacobi polynomials for spectral modeling of vector fields in polar coordinates

T. Sakai *, L.G. Redekopp

Department of Aerospace and Mechanical Engineering, University of Southern California, Los Angeles, CA 90089-1191, USA

A B S T R A C T

A spectral tau-method is proposed for solving vector field equations defined in polar coordinates. The method employs one-sided Jacobi polynomials as radial expansion functions and Fourier exponentials as azimuthal expansion functions. All the regularity requirements of the vector field at the origin and the physical boundary conditions at a circumferential boundary are exactly satisfied by adjusting the additional tau-coefficients of the radial expansion polynomials of the highest order. The proposed method is applied to linear and nonlinear-dispersive time evolution equations of hyperbolic-type describing internal Kelvin and Poincaré waves in a shallow, stratified lake on a rotating plane.

© 2009 Elsevier Inc. All rights reserved.

1. Introduction

Differential equations in physics are often described in a polar coordinate system. Such equations comprise coefficients varying as $1/r$ or $1/r^2$, and these terms are apparently singular at $r = 0$. When the equations, especially the nonlinear ones, are to be solved numerically, careful consideration must be given to these singularities so that the numerics can yield physically feasible solutions as $r \to 0$. The spectral methods, provided that the solution is expanded by appropriate polynomials, can yield smooth and bounded solutions, allowing one to simulate the physics of the problem without anxieties about having unphysical solutions near $r = 0$ at any time. For comprehensive discussions of spectral methods for problems with coordinate singularities, we refer to Chapter 18 in Boyd [5].

Physically well-behaved solutions in polar coordinates must satisfy a regularity condition that is solely a consequence of the coordinate transformation, independent of governing equations. In particular, an arbitrary scalar function ϕ defined in the polar coordinates (r, θ) is expanded in a Fourier series of the form

$$\phi(r, \theta) = \sum_{m=-\infty}^{\infty} \phi_m(r) e^{im\theta}. \tag{1}$$

* Corresponding author. Tel.: +1 213 740 9210.
  E-mail addresses: tsakai@usc.edu (T. Sakai), larrygre@usc.edu (L.G. Redekopp).

If $\phi(r, \theta)$ is analytic (C^{∞}) at $r = 0$, then in some vicinity of $r = 0$, $\phi_m(r)$ is expanded in a Taylor series of the form

$$\phi_m(r) = \sum_{k=0}^{\infty} \phi_{mn} r^{|m|+2k}, \tag{2}$$

where n is a cumulated radial modal index defined as $n = |m| + 2k$. This regularity condition is proved by writing the expansion (1) in terms of Cartesian coordinates (x, y) with $\phi_m(r)$ expanded by arbitrary powers of r, and requiring that all the terms are polynomial in x and y (e.g. see [5,7]). The best example of $\phi_m(r)$ is the Bessel function of the first kind $J_m(\lambda r)$, the radial eigenfunction of a Laplacian operator $\nabla^2 \phi = -\lambda^2 \phi$. The $J_m(\lambda r)$, having mth order zeros at $r = 0$ with the same parity as m (even or odd function about $r = 0$ depending on m being even or odd), is expanded exactly in the form of (2). Although such a Bessel function seems to be suitable for the expansion function, since the defining differential equation (Bessel's equation) is nonsingular at the outer boundary, the rate of convergence can be degraded, and the Gibb's phenomenon possibly emerges near the boundary (e.g. see [8, pp. 29–35]).

For the radial expansion function in a bounded domain, therefore, it is ideal that the function satisfies not only the regularity condition at $r = 0$, but also the defining differential equation is singular at the outer boundary [17]. The one-sided Jacobi polynomial, proposed independently by Matsushima and Marcus [17] and Verkley [23] for solving differential equations, satisfies these requirements. The one-sided Jaocbi polynomials have been used for seventy years in geometrical optics as the Zernike polynomials [25,4,19], and their applications are now numerous. In a scaled domain $0 \leqslant r \leqslant 1$, the one-sided Jacobi polynomial $Q_{mn}(r)$ is defined as

$$Q_{mn}(r) = r^{|m|} P_k^{(\alpha,\beta)}(2r^2 - 1), \tag{3}$$

where $P_k^{(\alpha,\beta)}(x)$ is the Jacobi polynomial (see [1, Section 22]) and α and β (both > -1) are arbitrary parameters. Since $P_k^{(\alpha,\beta)}(2r^2 - 1)$ is an even polynomial of degree $2k$, $Q_{mn}(r)$ is a polynomial containing powers $r^{|m|}, r^{|m|+2}, \cdots, r^{|m|+2k}$. This readily implies that $\phi_m(r)$ admits a direct expansion in terms of $Q_{mn}(r)$. Furthermore, noting the fact that $P_k^{(\alpha,\beta)}(x)$ is an orthogonal polynomial in $-1 \leqslant x \leqslant 1$ with respect to the weight $(1-x)^\alpha (1+x)^\beta$, the orthogonality relation is written as

$$\int_0^1 Q_{mn}(r) Q_{mn'}(r) w(r) dr = \frac{\delta_{nn'}}{2(2k + \alpha + \beta + 1)} \frac{\Gamma(k + \alpha + 1)\Gamma(k + \beta + 1)}{k! \Gamma(k + \alpha + \beta + 1)}, \tag{4}$$

and the weight function $w(r)$ is given by

$$w(r) = (1 - r^2)^\alpha r^{2(\beta - |m|)+1}. \tag{5}$$

Since the Jacobian for polar coordinates is r, the obvious choice is $\alpha = 0$ and $\beta = |m|$, the parameter set used by Matsushima and Marcus [17] and Verkley [23]. The choice of $\alpha = \beta = -1/2$ gives the polar-Robert functions $r^{|m|} T_k(2r^2 - 1) = r^{|m|} T_{2k}(r)$, where $T_k(x)$ is the Chebyshev polynomial of degree k. In contrast to the aforementioned Jacobi basis set, the polar-Robert bases are known to be severely ill-conditioned at larger truncations [18,5]. Recently Livermore et al. [15] proposed the polynomial with the new set $\alpha = -1/2$ and $\beta = |m| - 1/2$, the so called Worland polynomial in their paper. This particular set of parameters gives the weight function $1/\sqrt{1 - r^2}$, the same as that for Chebyshev polynomials. Their numerical experiments showed that both the original one-sided Jacobi and the Worland polynomials behaved similarly, but when approximating a boundary layer function, Worland polynomials achieved a smaller local error close to the boundary.

The one-sided Jacobi polynomials have been proven to work successfully for problems involving scalar functions. Matsushima and Marcus [17] and Livermore et al. [15] tested the one-sided Jacobi polynomials for Bessel's eigenvalue problem, and it was shown that a much faster convergence rate was achieved than when using Chebyshev polynomials for the expansion function. As for time-dependent problems Verkley [24] and Matsushima and Marcus [17] successfully applied the one-sided Jacobi polynomials for solving incompressible fluid dynamic equations in a disc. As demonstrated by their pioneer work, the use of the one-sided Jacobi polynomials as radial basis functions is particularly advantageous for explicitly advancing time-dependent problems, overcoming a severe time step restriction related to over-resolution near $r = 0$ (i.e. the pole problem), which frequently occur with use of conventional radial bases (e.g. Chebyshev polynomials) or finite difference methods.

Regarding problems involving vector functions, still only a few applications of the one-sided Jacobi polynomials exist. Since the regularity condition of the vector function is different from the scalar counterpart, some modification of the one-sided Jacobi basis is necessary. Leonard and Wray [13] used modified one-sided Jacobi polynomials, multiplying a factor $(1 - r^2)$ to satisfy the boundary condition at $r = 1$, and constructed a divergence-free velocity field for viscous flow in a pipe. Ishioka [9,10] modified the one-sided Jacobi polynomials in similar manner, and constructed Galerkin-type vector basis functions completely satisfying the regularity and boundary conditions for solving the shallow water equation in a disc. Recently Auteri and Quaterpelle [2,3] applied the one-sided Jacobi radial bases in their spectral-Galerkin solver for three-dimensional, scalar and vector elliptic-type equations in a sphere and in a finite cylinder, and then the spectral convergence of the solution algorithms was clearly demonstrated.

In fluid mechanics, flows inside a circular cylinder have long been of great interest, and accurate flow (vector) solvers are essential tools to investigate class of flows such as instabilities of boundary layers and turbulent flows. Incompressible Navier–Stokes equations have been solved in the past employing spectral methods with use of conventional polynomial bases for radial expansions. For example, Orszag and Patera [21] and Priymak and Miyazaki [22] used parity-restricted

Chebyshev polynomials for radial bases to expand the flow field in a periodic, circular pipe. Lopez et al. [16] used recombined Legendre polynomials for radial bases in their spectral-Galerkin flow solver in a finite cylinder. Primary advantage of using such conventional bases is that computationally efficient algorithms for highly-resolved flows can be constructed by exploiting already existing, successful subroutine libraries and flow solvers that are originally developed for cartesian coordinates. None of these applications, however, fully satisfy the regularity conditions of both vector and scalar field variables. Only essential conditions, that is, a few regularity conditions of the lowest modes, are satisfied to enforce the field variables and the divergence of the flow field be nonsingular on the center axis.

As shown in the next section, the expansion coefficients of radial (r) and azimuthal (θ) components of an analytic vector function are coupled to each other. For this reason, the expansion functions for radial and azimuthal vector components are designed necessarily in a coupled form as well. Adding requirements to satisfy the physical boundary conditions for the vector components, the resulting basis functions become complicated and, consequently, the Galerkin-type formulation and subsequent implementation become inevitably complicated. In this paper we propose a tau-method that allows one to keep using the original form of the one-sided Jacobi polynomial (3) for the radial basis functions. All the regularity conditions as well as physical boundary conditions are fully satisfied by adjusting the extra spectral (tau) coefficients. Through this approach, the coupling of the vector basis function is avoided, and the drawback of using Galerkin-type basis functions can be alleviated. Applications of the proposed method to hydrodynamic model equations are described in Sections 3 and 4.

2. Spectral representation of vector function

Since vectors are not invariant under the transformation between two coordinate systems, the regularity condition of the vector functions is essentially different from that of the scalar functions. This can be derived in many ways (e.g. see [14,9,20]). In what follows we summarize the results.

An arbitrary vector function $\mathbf{u} \equiv u\mathbf{e}_r + v\mathbf{e}_\theta$ defined in the polar coordinates (r, θ) is expanded in a Fourier series of the form

$$\mathbf{u}(r, \theta) = \sum_{m=-\infty}^{\infty} \mathbf{u}_m(r)e^{im\theta}. \tag{6}$$

If $\mathbf{u}(r, \theta)$ is analytic at $r = 0$, then in some vicinity of $r = 0$, $\mathbf{u}_m(r)$ is expanded in a Taylor series of the form

$$\mathbf{u}_m(r) = \sum_{k=0, n \geqslant 1}^{\infty} \mathbf{u}_{mn-1} r^{|m|+2k-1} = \sum_{k=0, n \geqslant 1}^{\infty} \mathbf{u}_{mn-1} r^{n-1}, \tag{7}$$

where $n = |m| + 2k$, and the leading coefficient $\mathbf{u}_{m|m|-1}$ satisfies the relation

$$u_{m|m|-1} + i\,\text{sgn}(m)\,v_{m|m|-1} = 0 \quad \text{for } |m| \geqslant 1. \tag{8}$$

It should be noted that in (7) there is a condition for the summation index k as implicitly given by $n \geqslant 1$. In particular, if $m = 0$, the radial index is $n = 2k$ and, then, k starts from 1 (not zero) such that the radial power $r^{2k-1}(= r^{n-1})$ is nonsingular at $r = 0$.

The radial expansion function $\mathbf{u}_m(r)$ has a base factor $r^{|m|-1}$, the opposite parity to the scalar counterpart (2). The relation (8) is a coupled constraint hidden in the analytic vector components, a so called the kinematic constraint [20]. Only satisfying the parity condition (7) does not guarantee the regularity of the vector function. Satisfying the kinematic constraint provides an important physical implication. For an instructive purpose, suppose that we compute the divergence of the vector field at $r = 0$,

$$\nabla \cdot \mathbf{u} = \frac{\partial u}{\partial r} + \frac{u}{r} + \frac{1}{r}\frac{\partial v}{\partial \theta}. \tag{9}$$

Substituting the expansion (6) and (7) into above expression, we have

$$\nabla \cdot \mathbf{u} = \sum_{m=-\infty}^{\infty} \sum_{k=0, n \geqslant 1}^{\infty} \{(|m| + 2k)u_{mn-1} + i m v_{mn-1}\} r^{|m|+2k-2} e^{im\theta}. \tag{10}$$

The lowest radial power is r^{-1} when $m = \pm 1$ and $k = 0$, and its coefficient is $u_{\pm 10} \pm i\,v_{\pm 10}$. These values are identically zero provided that the kinematic constraint (8) holds. Satisfying the kinematic constraint at $m = \pm 1$ guarantees that $\nabla \cdot \mathbf{u}$ is finite as $r \to 0$. But this is not sufficient to guarantee the regularity of $\nabla \cdot \mathbf{u}$ at $r = 0$. Noting the fact that the divergence is a scalar function, the radial components of $\nabla \cdot \mathbf{u}$ must be expanded in the form (2). The above expansion (10), therefore, must have an mth order zero. Since the lowest order term of (10) is $r^{|m|-2}$ when $k = 0$, its coefficient $|m|\{u_{m|m|-1} + i\,\text{sgn}(m)\,v_{m|m|-1}\}$ must vanish. This is accomplished by satisfying the kinematic constraint (8).

Field equations usually contain dependent variables of both scalar and vector forms. Since the power series in vector functions is one degree less than that in scalar functions, the radial expansion functions become different from the scalar counterparts. In order to use common radial basis functions for the vector and the scalar variables, we introduce a new vector function $\tilde{\mathbf{u}}$, a radial flux of $\mathbf{u}$ defined as

$$\tilde{\mathbf{u}}(r, \theta) \equiv r\mathbf{u} = \sum_{m=-\infty}^{\infty} \tilde{\mathbf{u}}_m(r)e^{im\theta}. \tag{11}$$

The corresponding radial expansion function $\tilde{\mathbf{u}}_m(r)$ is of the same parity as that of the scalar functions (7)

$$\tilde{\mathbf{u}}_m(r) = \sum_{k=0, n \geqslant 1}^{\infty} \tilde{\mathbf{u}}_{mn} r^{|m|+2k}, \tag{12}$$

where the radial index of $\tilde{\mathbf{u}}_{mn}$ is increased by one. Although the scalar functions contain a constant term if $m = 0$, $\tilde{\mathbf{u}}_m(r)$ does not contain such a constant term as a consequence of multiplication of r. The kinematic constraint is essentially the same as (8) with the radial indices increased by one, namely

$$\tilde{u}_{m|m|} + \mathrm{i}\,\mathrm{sgn}(m)\tilde{v}_{m|m|} = 0 \quad \text{for } |m| \geqslant 1. \tag{13}$$

The expansion functions in the tau-method do not necessarily satisfy the boundary conditions or even the kinematic constraint. Therefore, we require the radial expansion functions to satisfy only the parity condition (12). Using the one-sided Jacobi polynomial $Q_{mn}(r)$ defined by (3), $\tilde{\mathbf{u}}$ can be approximated by a finite series in a triangular truncation form

$$\tilde{\mathbf{u}}^N(r, \theta) = \sum_{m=-N}^{N} \sum_{n=|m|, n \geqslant 1}^{N+2\tau} \tilde{\mathbf{u}}_{mn}\left\{ Q_{mn}(r) - \delta_{m0}(-1)^k \frac{(\beta+1)_k}{k!} Q_{00}(r) \right\} e^{\mathrm{i}m\theta}, \tag{14}$$

where δ_{m0} is a Kronecker's delta, and $(\cdots)_k$ is a Pochhammer symbol defined as $(z)_k = \Gamma(z+k)/\Gamma(z)$. Note that the spectral coefficient $\tilde{\mathbf{u}}_{mn}$ is different from that defined in (12). If $m \neq 0$, the radial expansion function is $Q_{mn}(r)$, identical with that for the scalar functions. For $m = 0$, since the parity condition (12) does not allow constant terms, a constant contribution (i.e. $Q_{0n}(0) = (-1)^k(\beta+1)_k/k!$ as given by (58) in Appendix A) is subtracted from the original polynomial $Q_{0n}(r)$ (note the factor $Q_{00}(r) = 1$ in (14)). Using the orthogonality (4), the spectral coefficient $\tilde{\mathbf{u}}_{mn}$ is determined through an integral transformation

$$\tilde{\mathbf{u}}_{mn} = \frac{(2k+\alpha+\beta+1)k!\Gamma(k+\alpha+\beta+1)}{\pi\Gamma(k+\alpha+1)\Gamma(k+\beta+1)} \int_0^{2\pi} \int_0^1 \tilde{\mathbf{u}}^N(r, \theta) Q_{mn}(r) w(r) e^{-\mathrm{i}m\theta} \mathrm{d}r\mathrm{d}\theta, \tag{15}$$

where $n = |m| + 2k \,(= |m|, |m|+2, \ldots, N)$. This transformation formula is identical with the scalar function counterpart.

The radial expansion in (14) has extra τ-coefficients indexed as $n = N+2, N+4, \ldots, N+2\tau$. By adjusting these τ-coefficients, the kinematic constraint and the boundary conditions can be satisfied. Although the kinematic constraint is imposed only on the coefficients of $r^{|m|}$ terms in $\tilde{\mathbf{u}}_m(r)$, in the polynomial expansion (14) each of the polynomials $Q_{mn}(r)$ at given m contain the $r^{|m|}$ term. Specifically, the radial expansion function $\tilde{\mathbf{u}}_m(r)$ for given m ($|m| \geqslant 1$) can be expressed as

$$\tilde{\mathbf{u}}_m(r) = \sum_{n=|m|}^{N+2\tau} \tilde{\mathbf{u}}_{mn} Q_{mn}(r) = \sum_{n=|m|}^{N+2\tau} \tilde{\mathbf{u}}_{mn}\left\{ c_{mn}^{(0)} r^{|m|} + c_{mn}^{(2)} r^{|m|+2} + \cdots \right\}. \tag{16}$$

The coefficient $c_{mn}^{(0)}$ at the leading power $r^{|m|}$ hidden in $Q_{mn}(r)$ is readily obtained by using the polynomial expression of $Q_{mn}(r)$ given by (49) in Appendix A. Extracting only the coefficient of $r^{|m|}$ from (16) and denoting the coefficient as $\tilde{\mathbf{u}}'_{m|m|} \equiv \left(\tilde{u}'_{m|m|}, \tilde{v}'_{m|m|} \right)^T$, we have

$$\tilde{\mathbf{u}}'_{m|m|} = \sum_{n=|m|}^{N+2\tau} c_{mn}^{(0)} \tilde{\mathbf{u}}_{mn} = \sum_{n=|m|}^{N+2\tau} (-1)^k \frac{(\beta+1)_k}{k!} \begin{pmatrix} \tilde{u}_{mn} \\ \tilde{v}_{mn} \end{pmatrix} \equiv \begin{pmatrix} \tilde{u}'_{m|m|} \\ \tilde{v}'_{m|m|} \end{pmatrix}. \tag{17}$$

Applying now the kinematic constraint (13) to the vector components $\tilde{u}'_{m|m|}$ and $\tilde{v}'_{m|m|}$ above, we obtain the kinematic constraint corresponding to the Jacobi expansion (14) as

$$\sum_{n=|m|}^{N+2\tau} (-1)^k \frac{(\beta+1)_k}{k!} \{\tilde{u}_{mn} + \mathrm{i}\,\mathrm{sgn}(m)\tilde{v}_{mn}\} = 0 \quad \text{for } |m| \geqslant 1. \tag{18}$$

The physical boundary conditions can be expressed similarly in terms of the spectral coefficients. For example, suppose that we want to impose a Dirichlet boundary condition $u = 0$ at $r = 1$ (i.e. $\tilde{u} = 0$ at $r = 1$). Employing a property of the one-sided Jacobi polynomial (56) given in Appendix A, we have that

$$\sum_{n=|m|, n \geqslant 1}^{N+2\tau} \frac{1}{k!} \{(\alpha+1)_k - \delta_{m0}(-1)^k (\beta+1)_k\}\tilde{u}_{mn} = 0 \quad \text{for all } m. \tag{19}$$

The radial truncation limit ($n = N + 2\tau$) depends on the number of physical boundary conditions. For example, if the boundary condition is imposed on either u or v, the radial truncation limit should be chosen at $N + 2$; that is, the boundary condition is satisfied by adjusting $\tilde{u}_{mN+2}$ (or $\tilde{v}_{mN+2}$), and the kinematic constraint (18) is satisfied by adjusting $\tilde{v}_{mN+2}$ (or $\tilde{u}_{mN+2}$). If the boundary condition is imposed on both u and v, the radial truncation limit should be chosen at $N + 4$.

With the expansion (14), the physical value $\mathbf{u}^N$, computed by dividing $\tilde{\mathbf{u}}^N$ by r, is in turn numerically singular at $r = 0$. Practically, however, this is not a problem. The vector $\mathbf{u}$ at $r = 0$ is multi-valued (in θ-direction) due to the nature of the polar

coordinates, and such values are not usually needed in the spectral methods (e.g. Gauss–Radau or Gauss–Legendre type radial collocation grids exclude the point $r = 0$). It is possible to use the crude vector form $\mathbf{u}$ that can be expanded by using the one-sided Jacobi polynomials (e.g. $\mathbf{u}_m(r) \sim r^{|m|-1} P_k^{(\alpha,\beta)}(2r^2 - 1)$ for $m \neq 0$ with use of the weight $w(r) = r^3$ for the inner product). However, employing the radial flux form $\tilde{\mathbf{u}}$ is rather more advantageous computationally. As mentioned above, the radial expansion functions of $\tilde{\mathbf{u}}$ given by (14) are the same as those of the scalar functions except only $m = 0$ and, also noting the fact that their radial derivatives are identical, one can simplify the computer program and save the computer memory by defining common basis matrices.

3. Linear evolution model

We first apply the tau-method to a linear, hyperbolic-type evolution model that has been frequently used to study the hydrodynamics of large lakes. The equation set is given by

$$
\begin{aligned}
&\frac{\partial U}{\partial t} - \mathcal{B}V + c^2 \frac{\partial Z}{\partial r} = 0, \\
&\frac{\partial V}{\partial t} + \mathcal{B}U + c^2 \frac{1}{r} \frac{\partial Z}{\partial \theta} = 0, \\
&\frac{\partial Z}{\partial t} + \frac{\partial U}{\partial r} + \frac{U}{r} + \frac{1}{r} \frac{\partial V}{\partial \theta} = 0.
\end{aligned}
\tag{20}
$$

Here we denote the dependent variables: the amplitudes of the radial velocity U, the azimuthal velocity V, and the isopycnal surface Z. $(U, V)^T$ is a vector, and Z is a scalar field. c is a linear wave phase speed, and $\mathcal{B}$ is called the Burger number, a parameter defining the effect of Coriolis acceleration. We solve the model equation in a unit disc under the slip-free boundary condition ($U = 0$ at $r = 1$).

3.1. Spectral formulation

Before presenting results we describe the spectral formulation of the problem based on the tau-method. Introducing the radial flux of the vector field defined by the relation $(\tilde{U}, \tilde{V})^T = r(U, V)^T$, the Eq. (20) is written in the form:

$$
\frac{\partial \tilde{U}}{\partial t} = R^{(u)}; \quad \frac{\partial \tilde{V}}{\partial t} = R^{(v)}; \quad \frac{\partial Z}{\partial t} = R^{(z)}.
\tag{21}
$$

The approximated solution set $\{\tilde{U}^N, \tilde{V}^N, Z^N\}$ is sought in a truncated series of the form:

$$
Z^N = \sum_{m=-N}^{N} \sum_{n=|m|}^{N} z_{mn} X_{mn}(r, \theta), \quad \begin{pmatrix} \tilde{U}^N \\ \tilde{V}^N \end{pmatrix} = \sum_{m=-N}^{N} \sum_{n=|m|, n \geqslant 1}^{N+2} \begin{pmatrix} u_{mn} \\ v_{mn} \end{pmatrix} Y_{mn}(r, \theta),
\tag{22}
$$

where the expansion functions X_{mn} and Y_{mn} are defined as

$$
X_{mn}(r, \theta) = Q_{mn}(r) e^{im\theta}, \quad Y_{mn}(r, \theta) = \{Q_{mn}(r) - \delta_{m0}(-1)^k\} e^{im\theta}.
\tag{23}
$$

$Q_{mn}(r)$ is a one-sided Jacobi polynomial with a particular choice $(\alpha, \beta) = (0, |m|)$ written explicitly here as

$$
Q_{mn}(r) = r^{|m|} P_k^{(0,|m|)}(2r^2 - 1),
\tag{24}
$$

where $n = |m| + 2k$ with $k = 0, 1, 2, \ldots$. Note that the scalar field Z is directly expanded by $Q_{mn}(r)$, and that the vector field $(\tilde{U}, \tilde{V})^T$ is expanded in the form of (14) in the previous section. The constant $\delta_{m0}(-1)^k$ in the definition of Y_{mn} in (23) is obtained after substituting $(\alpha, \beta) = (0, |m|)$ into (14) (i.e. $\delta_{m0}(-1)^k(|m| + 1)_k/k! = \delta_{m0}(-1)^k(1)_k/k! = \delta_{m0}(-1)^k$). N represents a truncation limit for the azimuthal mode. The truncation limit of the radial mode for Z is also N. The radial truncation limit for the vector field is chosen to be $N + 2$ in order to satisfy the boundary condition and the kinematic constraint with the spectral coefficients of the highest order.

We define an inner product in the form

$$
\langle X, Y \rangle \equiv \frac{1}{2\pi} \int_0^{2\pi} \int_0^1 XY^* r \, dr \, d\theta,
\tag{25}
$$

where the upper script (*) denotes the complex conjugate. Orthogonality identities of X_{mn} and Y_{mn} are given by

$$
\begin{aligned}
&\langle X_{mn}, X_{m'n'} \rangle = \frac{\delta_{mn'} \delta_{nn'}}{2(n+1)}, \\
&\langle Y_{mn}, X_{m'n'} \rangle = \langle X_{mn}, X_{m'n'} \rangle \quad \text{if } n \neq 0.
\end{aligned}
\tag{26}
$$

Substituting the expansion (22) into (21), and taking the inner product with respect to $X_{mn}^*(r, \theta)$, we obtain, after using the orthogonality (26), a set of ordinary differential equations (ODEs) for u_{mn}, v_{mn} and z_{mn}.

For given m, we have equations for $n = |m|, |m| + 2, \ldots N$ to determine du_{mn}/dt and dv_{mn}/dt as following

$$\frac{du_{mn}}{dt} = 2(n+1)\langle R^{(u)N}, X_{mn} \rangle,$$
$$\frac{dv_{mn}}{dt} = 2(n+1)\langle R^{(v)N}, X_{mn} \rangle. \tag{27}$$

In this expression, $R^{(\cdots)N}$ denotes an approximation of $R^{(\cdots)}$ calculated using the approximated solution (22). To describe how to satisfy both the physical boundary condition and the kinematic constraint, we suppose $m \neq 0$ here unless as otherwise noted.

The physical boundary condition ($\widetilde{U} = 0$ at $r = 1$) is satisfied by adjusting the highest coefficient u_{mN+2}. Differentiating with respect to t the expression of the boundary condition (19) with $(\alpha, \beta) = (0, |m|)$, we have

$$\sum_{n=|m|, \, n \geqslant 1}^{N+2} \{1 - \delta_{m0}(-1)^k\} \frac{du_{mn}}{dt} = 0. \tag{28}$$

Since du_{mn}/dt are explicitly determined from the first equation in (27) for $n \leqslant N$, du_{mN+2}/dt is explicitly determined from the boundary condition (28).

Next, the kinematic constraint is satisfied by adjusting the highest coefficient v_{mN+2}. Differentiating with respect to t the kinematic constraint (18) with $(\alpha, \beta) = (0, |m|)$, we have

$$\sum_{n=|m|}^{N+2} (-1)^k \frac{(|m|+1)_k}{k!} \left\{ \frac{du_{mn}}{dt} + i\,\mathrm{sgn}(m) \frac{dv_{mn}}{dt} \right\} = 0 \quad \text{for } m \neq 0. \tag{29}$$

Since values of du_{mn}/dt are now all known and values of dv_{mn}/dt are determined by the second equation in (27) for $n \leqslant N$, dv_{mN+2}/dt is explicitly determined from the kinematic constraint (29).

For $m = 0$, we have the same equation set (27) for $\widetilde{U}$ and $\widetilde{V}$. Similarly the boundary condition is satisfied by the highest coefficient in (28). The values of dv_{0n}/dt are explicitly determined from (27) for all n and, therefore, the imposition of the kinematic constraint is unnecessary. The values of dz_{mn}/dt are determined explicitly for all m and n by the equation similar to the vector field

$$\frac{dz_{mn}}{dt} = 2(n+1)\langle R^{(z)N}, X_{mn} \rangle. \tag{30}$$

The values of du_{mn}/dt, dv_{mn}/dt and dz_{mn}/dt are now all determined, and these values can be integrated forward-in-time through an appropriate ODE integration scheme. In this study we used the fixed time step, fourth-order Runge–Kutta method.

Since the present numerical method was originally developed for solving nonlinear equations being presented in the following section, the inner products in (27) and (30) were numerically evaluated. Numerical evaluation of the inner products involving nonlinear terms is described in Section 4. At each time step, after integrating u_{mn}, v_{mn} and z_{mn}, the solution in the physical space is computed by (22) through the basis matrix multiplication. The radial derivatives of the solution are computed by (22) with the basis replaced by its derivative that is computed by the formula given in Appendix A. The values $R^{(u)N}$, $R^{(v)N}$ and $R^{(z)N}$ are then obtained at the physical collocation grid, and then their inner products are readily computed.

The analytical solution to the evolution system (20) is described in [12, pp. 317–324] and in [6]. Writing the solution in the form of the radial velocity flux field (i.e. $(\widetilde{U}, \widetilde{V})^T = r(U, V)^T$),

$$\widetilde{U} = -A_0 \frac{c^2}{\mathcal{B}(\omega^2 - 1)} \widetilde{U}_m(r) \sin(m\theta - \mathcal{B}\omega t),$$
$$\widetilde{V} = A_0 \frac{c^2}{\mathcal{B}(\omega^2 - 1)} \widetilde{V}_m(r) \cos(m\theta - \mathcal{B}\omega t), \tag{31}$$
$$Z = A_0 Z_m(r) \cos(m\theta - \mathcal{B}\omega t),$$

where A_0 is a wave amplitude, $m\,(> 0)$ is an azimuthal wave-number, and radial functions $\widetilde{U}_m(r)$ and $\widetilde{V}_m(r)$ are written as

$$\widetilde{U}_m(r) = m Z_m(r) - \omega r Z_m'(r),$$
$$\widetilde{V}_m(r) = m\omega Z_m(r) - r Z_m'(r). \tag{32}$$

The radial eigenfunction $Z_m(r)$ is normalized by its maximum value; that is, $Z_m(r) = Z_m^*(r)/|Z_m^*(r)|_{\max}$, and $Z_m^*(r)$ is either the Bessel (J) or the modified-Bessel (I) function depending on the value of ω

$$\mathcal{Z}_m^*(r) = \begin{cases} I_m(\mathcal{B}^* r) & \text{if } \omega^2 < 1, \\ J_m(\mathcal{B}^* r) & \text{if } \omega^2 > 1, \end{cases} \quad \text{and } \mathcal{B}^* = \frac{\mathcal{B}}{c}\sqrt{|1 - \omega^2|}. \tag{33}$$

The solution corresponding to $\omega^2 < 1$ is characterized as the Kelvin wave, and that corresponding to $\omega^2 > 1$ is characterized as the Poincaré wave. Radial wave-number $\lambda = \mathcal{B}^*$ is implicitly defined through ω, which is the eigenfrequency determined by the dispersion relation. For the Poincaré wave mode, the eigenfrequency is given by the transcendental relation

$$\lambda J_{m-1}(\lambda) - m\left(1 + \frac{1}{\omega}\right) J_m(\lambda) = 0. \tag{34}$$

This equation is readily solved by the half-interval method. For the Kelvin wave mode ($\omega^2 < 1$), the J-Bessel function is replaced with the I-Bessel function in (34).

We distinguish the wave traveling direction by calling 'cyclonic' (counter clockwise rotation) for positive frequency ($\omega > 0$) and 'anti-cyclonic' for negative frequency ($\omega < 0$). For convention, we label the fundamental wave mode through a format 'M(azimuthal mode)R(radial mode)' with the sign plus (+) for cyclonic or negative (−) for anti-cyclonic wave mode.

Since the I-Bessel function possesses the same parity as that of the J-Bessel function, the radial eigenfunction $Z_m(r)$ fully satisfies the regularity condition (2). Also, using the series expansions for Bessel functions and complex exponentials for trigonometric functions, it can be easily verified that the coefficient of the leading term r^{m-1} of the exact solution $(U, V)^T$ fully satisfies both the parity condition (7) and the kinematic constraint (8).

The exact solution can be expanded by $Q_{mn}(r)$ analytically (see Appendix B). In particular, the radial functions of unscaled form $\left\{ \widetilde{U}_m^*, \widetilde{V}_m^*, Z_m^* \right\}$ for the Poincaré wave mode are expressed as

$$\widetilde{U}_m^*(r) = \frac{2}{\lambda} \sum_{k=0}^{\infty} (-1)^k (n+1)\{[(1+\omega)m + 2\omega(k+1)]J_{n+1}(\lambda) - \lambda\omega J_n(\lambda)\}Q_{mn}(r),$$

$$\widetilde{V}_m^*(r) = \frac{2}{\lambda} \sum_{k=0}^{\infty} (-1)^k (n+1)\{[(1+\omega)m + 2(k+1)]J_{n+1}(\lambda) - \lambda J_n(\lambda)\}Q_{mn}(r), \tag{35}$$

$$Z_m^*(r) = \frac{2}{\lambda} \sum_{k=0}^{\infty} (-1)^k (n+1)J_{n+1}(\lambda)Q_{mn}(r),$$

where $n = m + 2k$. The Kelvin wave counterpart has a similar form with J-Bessel function replaced with I-Bessel function and omitting the factor $(-1)^k$ in the above expression. An asymptotic expression of J-Bessel function given by 9.3.1 in [1] is

$$J_n(x) \sim \frac{1}{\sqrt{2\pi n}} \left(\frac{ex}{2n} \right)^n \quad \text{for } n \to \infty \text{ with } x \text{ fixed}. \tag{36}$$

This expression implies that the expansion coefficients of the radial functions (35) have the property of infinite order, providing the spectral convergence. This is also true for the Kelvin wave solutions because the identity $I_n(x) = (-i)^n J_n(ix)$ yields the same asymptotic relation as (36).

3.2. Simulation results

The spectral method described above was implemented in a computer program written in FORTRAN90, and numerical computation was performed in double precision arithmetic. A truncated form of the exact solution (35) was used as the initial value for the spectral evolution Eqs. (27) and (30). Parameters chosen for the example runs are at $\mathcal{B} = 4$ and $c = 0.9394668213$. An exact solution of the isopycnal amplitude Z for the anti-cyclonic Poincaré wave of azimuthal mode one and radial mode one (M1R1−) is presented in Fig. 1(a). Solutions presented in the figure are all normalized by the (initial) wave amplitude A_0. This initial solution field starts to rotate anti-cyclonically around $r = 0$ at a constant frequency without changing its spatial structure. In the same figure, numerical solutions of both the isopycnal and the velocity amplitude fields at $t = 13.75$ are presented. At this time the field rotated around the center ten times. The spectral truncation was chosen at $N = 5$ with the time step $\Delta t = 0.005$, although much larger time step is permissible for stable time integration. The solution field at $t = 13.75$ is very close to the exact solution qualitatively. At this truncation only two one-sided Jacobi modes are contained in the spectral approximation of Z at $m = 1$. In Fig. 2 a similar comparison is presented for the anti-cyclonic Poincaré wave of azimuthal mode three and radial mode three (M3R3−). The solution field is compared at $t = 5.475$ corresponding to approximately ten local oscillation periods ($10 \times 2\pi/\mathcal{B}\omega$) or three and one-third wave rotations. The spectral
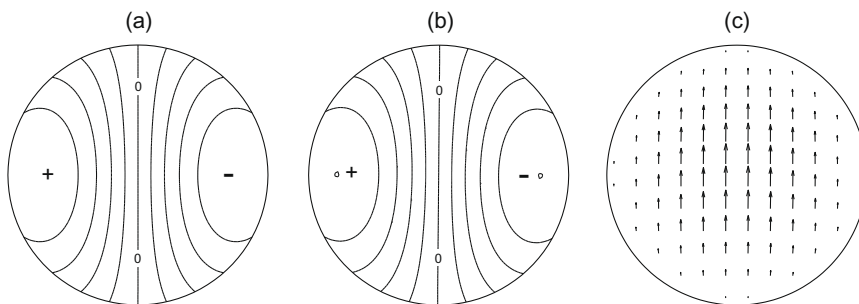

Fig. 1. Exact solution of the isopycnal amplitude Z for M1R1− wave mode at $t = 0$ (a), numerical solution at $t = 13.75$ (b), and corresponding vector field (c) obtained with the spectral truncation $N = 5$. Contour level step is 0.2.
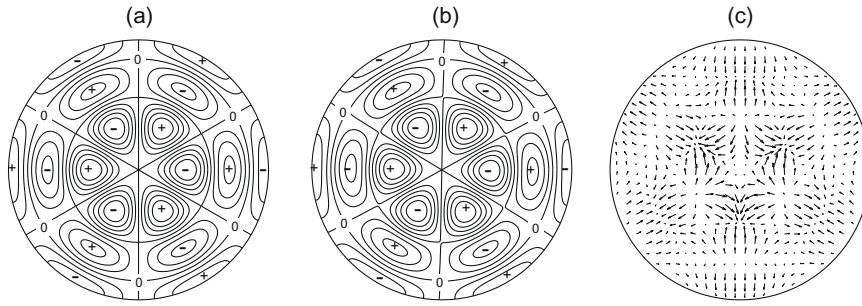
Fig. 2. Exact solution of the isopycnal amplitude Z for M3R3− wave mode at $t = 0$ (a), numerical solution at $t = 5.475$ (b), and corresponding vector field (c) obtained with the spectral truncation $N = 15$. Contour level step is 0.2.

Table 1
Instantaneous error of isopycnal amplitude Z at $t = 5.475$ sampled at different radial locations for various truncation limit N for time integration with M3R3− wave mode. Values are normalized by the initial wave amplitude. Values in parentheses in $r = 0.35$ column are obtained with a halved time step $\Delta t = 0.0025$.

N	$r = 0.35$	$r = 0.7$	$r = 1$
10	7.24×10^{-1} (7.24×10^{-1})	5.49×10^{-1}	7.70×10^{-2}
15	9.48×10^{-3} (9.72×10^{-3})	2.19×10^{-4}	4.37×10^{-3}
20	6.44×10^{-5} (6.65×10^{-5})	2.45×10^{-5}	3.56×10^{-5}
25	3.96×10^{-7} (3.46×10^{-9})	2.79×10^{-7}	2.19×10^{-7}
30	4.11×10^{-7} (1.73×10^{-8})	2.78×10^{-7}	2.29×10^{-7}

truncation in this example was chosen at $N = 15$ with $\Delta t = 0.005$. Although the spatial structure of the solution field is more complicated than the previous example, at this truncation only six one-sided Jacobi modes are present in the spectral approximation of Z at $m = 3$. Again, the solution field at $t = 5.475$ is already very close to the exact solution qualitatively.

In order to quantify the fast convergence of the numerical solutions, local error of the isopycnal amplitude was sampled at different radial locations on the horizontal axis ($\theta = 0$) at a fixed time for various truncation limits. The results for the M3R3− wave mode at $t = 5.475$ are shown in Table 1. The sampling locations were chosen at $r = 0.35, 0.7$ and 1, and these locations are very close to either the local maxima or minima of the isopycnal amplitude field (see Fig. 2). The error values decrease uniformly and exponentially fast up to the $N = 25$ (N25) truncation limit, and they converge to some values of certain order regardless of increasing the truncation limit. For large truncation limit the gross numerical error can become dominated by the time discretization error. In fact, when halving the time step size to $\Delta t = 0.0025$, the numerical errors at N25 and N30 decrease as supplemented in Table 1. Reducing the time step size for small truncation limit does not help reduce the error at all, implying that the spatial descretization error is rather dominant in the gross error. Hence, the numerical error can decrease exponentially fast as a function of the truncation limit, provided the time step size is sufficiently small.

For the next validation we examine the global error of the numerical solutions by calculating conserved quantities of the system (20). The spatial integrals of the isopycnal amplitude (M), the relative vorticity (W) and the total energy (E) are conserved quantities defined as following

$$M = \int_0^{2\pi} \int_0^1 Z r \, dr \, d\theta,$$
$$W = \int_0^{2\pi} \int_0^1 \left\{ \frac{\partial V}{\partial r} + \frac{V}{r} - \frac{1}{r} \frac{\partial U}{\partial \theta} \right\} r \, dr \, d\theta,$$
$$E = \int_0^{2\pi} \int_0^1 \frac{1}{2} \{ U^2 + V^2 + c^2 Z^2 \} r \, dr \, d\theta.$$
$$(37)$$

The integral isopycnal amplitude M is always conserved in the method presented here. The isopycnal amplitude Z is time integral of the divergence of the velocity field (see (20)). According to the Gauss divergence theorem, and recalling the normal velocity vanishing boundary condition ($U = 0$ at $r = 1$), the surface integral of the divergence field is identically zero (alt. $M = 0$). The present numerical method exactly satisfies the boundary condition through the spectral tau-equation (28), guaranteeing $M = 0$ at all times. The integral vorticity W and the energy E, however, are not conserved in the present method. Although the azimuthal expansion with Fourier modes helps the integral vorticity be conserved except at the zero-th azimuthal mode ($m = 0$), the energy, as a quadratic quantity, is not conserved at all azimuthal modes. The evolution equations for the tau-coefficients (28) and (29) are different from the spectral evolution Eq. (27) projected from the original system Eq. (20). Hence, the present method seeks for the solutions to the modified equations, a nature of the tau-method [8,5].

Although the present method renders the numerical scheme non-conservative, the deviation of the conserved quantities diminish as fast as the numerical solution converges. To demonstrate this statement, the integral energy E was calculated at different times for various truncation limits for the time integration with M1R1− (Table 2) and M3R3− (Table 3) wave modes. The integration time step was fixed at $\Delta t = 0.005$. All the energy values are normalized by the initial value at

Table 2
Energy *E* computed at different time for various truncation limits *N* for time integration with M1R1− wave mode. Values are normalized by their initial values at *t* = 0.

N	t = 1	t = 3	t = 6
5	1.0002782417	0.9995259713	1.0003938509
10	1.0000001149	1.0000000043	1.0000000093
15	0.9999999998	0.9999999988	0.9999999976
20	0.9999999998	0.9999999988	0.9999999976

Table 3
Energy *E* computed at different time for various truncation limits *N* for time integration with M3R3− wave mode. Values are normalized by their initial values at *t* = 0.

N	t = 1	t = 2	t = 3
10	2.4267690168	3.0829407465	2.1702447582
15	0.9945572323	0.9945807190	0.9974414656
20	0.9999898056	0.9999872125	1.0000006896
25	0.9999999502	0.9999998006	0.9999997031
30	0.9999999506	0.9999998023	0.9999997034

t = 0. It is evident from these tables that the energies uniformly converge exponentially fast up to values of certain order. The convergence rate of the M1R1− wave mode is much faster than that of the more complicated M3R3− wave mode. Increasing the truncation limit does not continually diminish the energy deviations because the time descretization error dominates in the larger truncation limit as suggested above. A more detailed example of the effect of the time step size and the truncation limit is presented in Table 4, where the energy *E* of the M1R1− wave mode at *t* = 5 for the time integration in different truncation limits are tabulated for several time step sizes. It is evident from the table that the spectral convergence to an exact value (unity) is achieved only if the time step size is sufficiently small (e.g. $\Delta t = 0.01$ gives exponential convergence up to N10 truncation, but at reducing the time step to $\Delta t = 0.001$ increases the convergence limit to N20).

The actual, maximum time step Δt_{max} for stable integrations for the time integration with M1R1− wave mode is shown in Fig. 3 as a function of the truncation limit *N*. From this figure it can be observed that the maximum time step is $O(N^{-2})$ for

Table 4
Energy *E* at *t* = 5 obtained at different truncation limits *N* for various time step sizes Δt for time integration with M1R1− wave mode. Values are normalized by their initial values at *t* = 0. No-value (−) implies that the time integration is unstable due to excessive time step size.

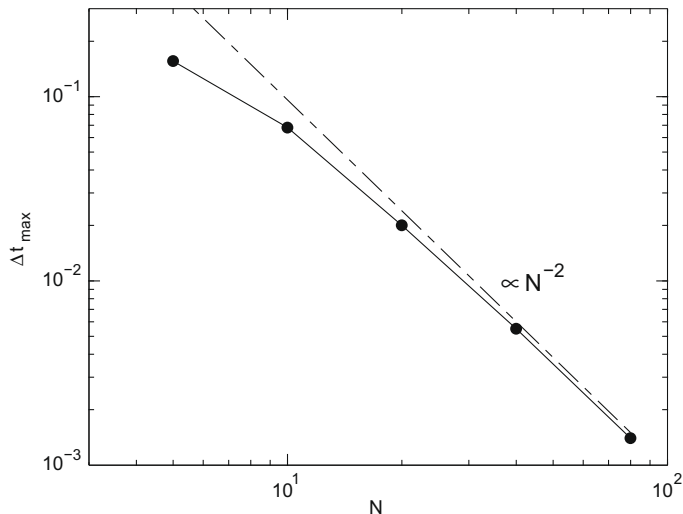| Δt	N = 5	N = 10	N = 20
0.1	0.9937544325	−	−
0.05	0.9997005005	0.9998037882	−
0.01	0.9999750209	0.9999999218	0.9999999368052
0.005	0.9999752403	0.9999999763	0.9999999980248
0.001	0.9999752525	0.9999999863	0.9999999999994

Fig. 3. Maximum allowable time step Δt_{max} for stable integration as a function of truncation limit *N* (M1R1− wave mode).

large N. This trend is related to high-wave-number oscillations of the radial bases close to the boundary $r = 1$, where the distance of the zeros of the highest-degree basis $P_{N/2}^{(0,0)}(2r^2 - 1)$ is also $O(N^{-2})$ [5,10]. Noting that there is no efficient transform method for the Jacobi bases, such a time-stiffness trend may become a restriction for high-spectral resolution time integrations, as one may seek for a potential use of the Chebyshev polynomials which offer efficient (Fast-Fourier-Cosine) transforms. Nevertheless, we appeal the fact that the Jacobi radial bases provide much faster convergence rate than the Chebyshev bases as demonstrated by many examples in the past, and that the former bases can satisfy all the regularity conditions at $r = 0$, which is not possible with the later bases.

4. Nonlinear evolution

4.1. Model formulation and algorithmic approach

The next example we apply the method to is a weakly-nonlinear, weakly-dispersive evolution model that is an asymptotic derivation based on the nonlinear system whose linearized reduction yields the linear model presented in the previous section. The asymptotic projection allows the elimination of the vertical structure, yielding a nonlinear system for the evolution of the horizontal structure of a specific vertical eigenmode. The equation set we study is given

$$
\frac{\partial U}{\partial t} - \mathcal{B}V + c^2\frac{\partial Z}{\partial r} = -\left\{\alpha\left(U\frac{\partial U}{\partial r} + \frac{V}{r}\frac{\partial U}{\partial \theta} - \frac{V^2}{r}\right) + \beta DU\right\} + \mu^2\gamma\frac{\partial}{\partial t}\left(\frac{\partial D}{\partial r}\right),
$$
$$
\frac{\partial V}{\partial t} + \mathcal{B}U + \frac{c^2}{r}\frac{\partial Z}{\partial \theta} = -\left\{\alpha\left(U\frac{\partial V}{\partial r} + \frac{V}{r}\frac{\partial V}{\partial \theta} + \frac{UV}{r}\right) + \beta DV\right\} + \mu^2\gamma\frac{\partial}{\partial t}\left(\frac{1}{r}\frac{\partial D}{\partial \theta}\right), \tag{38}
$$
$$
\frac{\partial Z}{\partial t} + \frac{\partial U}{\partial r} + \frac{U}{r} + \frac{1}{r}\frac{\partial V}{\partial \theta} = -\left\{\beta\left(U\frac{\partial Z}{\partial r} + \frac{V}{r}\frac{\partial Z}{\partial \theta}\right) + \alpha DZ\right\},
$$

where D is the horizontal divergence of the velocity field

$$
D = \frac{\partial U}{\partial r} + \frac{U}{r} + \frac{1}{r}\frac{\partial V}{\partial \theta}, \tag{39}
$$

and α, β, μ and γ are constant coefficients. The linear phase speed c and the Burger number $\mathcal{B}$ were kept at the same values as those in the previous section ($c = 0.9394668213$; $\mathcal{B} = 4$), and the additional coefficients were chosen as $\alpha = -0.3690737980, \beta = -0.1845368990, \gamma = 2.007821008$ and $\mu = 1/40$, which correspond to a specific stratified lake configuration. The solutions to the equation set are sought in a unit disc with the physical boundary condition $U = 0$ at $r = 1$. Besides nonlinear terms, the velocity equations contain dispersive terms consisting of the time derivative of the second spatial derivatives of velocity variables. Except handling of the dispersive terms, the numerical formulation is similar to that of the linear model discussed in the previous section.

Transforming the velocity field via the relation $(\widetilde{U}, \widetilde{V})^T = r(U, V)^T$, we write the equation in the form:

$$
\frac{\partial \widetilde{U}}{\partial t} = R^{(u)} + \frac{\partial}{\partial t}\left\{\mathcal{L}_r^{(u)}\widetilde{U} + \mathcal{L}_r^{(v)}\widetilde{V}\right\},
$$
$$
\frac{\partial \widetilde{V}}{\partial t} = R^{(v)} + \frac{\partial}{\partial t}\left\{\mathcal{L}_\theta^{(u)}\widetilde{U} + \mathcal{L}_\theta^{(v)}\widetilde{V}\right\}, \tag{40}
$$
$$
\frac{\partial Z}{\partial t} = R^{(z)},
$$

where $\mathcal{L}_r^{(\cdots)}$ and $\mathcal{L}_\theta^{(\cdots)}$ are linear operators for the dispersive terms. Spectral evolution equations of the velocity field are now coupled in the radial modal space due to the dispersive terms. The velocity equations in the spectral space are written in the form:

$$
\frac{du_{mn}}{dt} - \frac{d}{dt}\sum_{n'=|m|, n\geqslant 1}^{N+2}\left\{a_{mn,n'}^{(u)}u_{mn'} + a_{mn,n'}^{(v)}v_{mn'}\right\} = 2(n+1)\langle R^{(u)N}, X_{mn}\rangle,
$$
$$
\frac{dv_{mn}}{dt} - \frac{d}{dt}\sum_{n'=|m|, n\geqslant 1}^{N+2}\left\{b_{mn,n'}^{(u)}u_{mn'} + b_{mn,n'}^{(v)}v_{mn'}\right\} = 2(n+1)\langle R^{(v)N}, X_{mn}\rangle, \tag{41}
$$

for $n = |m|, |m| + 2, \ldots, N$. The constant $a_{mn,n'}^{(\cdots)}$ is defined by

$$
a_{mn,n'}^{(\cdots)} = 2(n+1)\int_0^1 Q_{mn}(r)\mathcal{L}_{r,m}^{(\cdots)}\{Q_{mn'}(r) - \delta_{m0}(-1)^k\}r dr, \tag{42}
$$

where $\mathcal{L}_{r,m}^{(\cdots)}$ is a linear operator for azimuthal mode m. Another constant $b_{mn,n'}^{(\cdots)}$ is defined in the same way with $\mathcal{L}_{r,m}^{(\cdots)}$ replaced with $\mathcal{L}_{\theta,m}^{(\cdots)}$. The integrals were evaluated exactly through the Gaussian quadrature.

Combining the evolution Eq. (41), the boundary condition (28), and the kinematic constraint (29), one can construct a linear system for du_{mn}/dt and dv_{mn}/dt in the form:

$$
\mathbf{A}_m\frac{d\mathbf{v}_m}{dt} = \mathbf{b}_m. \tag{43}
$$

In this equation, $\mathbf{A}_m$ is a system matrix, the vector $\mathbf{v}_m$ consists of all sets of $(u_{mn}, v_{mn})^T$ for given m, and the vector $\mathbf{b}_m$ consists of the right hand side of (41), (28) and (29). The size of $\mathbf{A}_m$ for arbitrary $m \, (\neq 0)$ is $(2\lfloor (N - |m|)/2\rfloor + 4) \times (2\lfloor (N - |m|)/2\rfloor + 4))$, where $\lfloor \cdots \rfloor$ denotes the floor function (i.e. $\lfloor x \rfloor$ gives the largest integer less than or equal to x). The inverse matrices $\mathbf{A}_m^{-1}$ are computed for all m before starting the time integration, and they are multiplied to $\mathbf{b}_m$ to determine $d\mathbf{v}_m/dt$ at every time step.

Inner products on the right hand side of the Eq. (41), now involving nonlinear terms, are numerically evaluated in accordance with the same philosophy described in [24]. To be specific to our problem, we write an inner product in the form

$$\langle R^{(u)N}(r, \theta), X_{mn}(r, \theta)\rangle = \int_0^1 R_m^{(u)N}Q_{mn}(r)rdr. \tag{44}$$

Here $R_m^{(u)N}(r)$ is an inner product of $R^{(u)N}$ with respect to $e^{-im\theta}$ defined as

$$R_m^{(u)N}(r) = \frac{1}{2\pi} \int_0^{2\pi} R^{(u)N}(r, \theta)e^{-im\theta}d\theta. \tag{45}$$

Since the maximum wave-number of the integrand is $3N$ (i.e. $2N$ for $R^{(u)N}$ and N for $e^{-im\theta}$), the integral (45) is calculated exactly through a discrete Fourier transform

$$R_m^{(u)N}(r) = \frac{1}{K} \sum_{k=1}^K R^{(u)N}(r, \theta_k)e^{-im\theta_k}, \tag{46}$$

where $\theta_k = (2\pi/K)(k - 1)$ and $K \geqslant 3N + 1$. This transform can be computed efficiently employing the fast Fourier transform. In this study we chose the value of K at a power of 2. After obtaining $R_m^{(u)N}(r)$, the radial integral in (44) is evaluated through the Gauss–Legendre type quadrature. Since (44) is an integral with respect to the weight r, it is convenient to use zeros of a Jacobi polynomial of the form $P_n^{(1,0)}(x)$ for the abscissas [11]. The quadrature formula is written explicitly as

$$\int_0^1 R_m^{(u)N}(r)Q_{mn}(r)rdr = \sum_{l=1}^L R_m^{(u)N}(r_l)Q_{mn}(r_l)w_l, \tag{47}$$

where r_l is the lth zero of $P_L^{(1,0)}(1 - 2r)$, and corresponding weight w_l is given by

$$w_l = \frac{1}{4r_l^2\left[P_L^{(1,0)'}(1 - 2r_l)\right]^2}. \tag{48}$$

Since the maximum degree of the polynomial in the integrand is $3N + 4$ (i.e. $2N + 2$ for $R_m^{(u)N}$ and $N + 2$ for Q_{mn}), the quadrature formula (47) is exact, provided $L \geqslant (3N + 5)/2$.

4.2. Simulation results

For numerical examples we consider the evolution of the initial value defined by (32) in the previous section. Although the solution (32) now becomes only a leading order, asymptotic solution (at vanishing amplitude) to the present nonlinear model (38), it is still interesting to see whether the model is stably integrated for a long-time yielding physically reasonable solutions through the proposed numerical method.

In Fig. 4 an evolution of the azimuthal mode one Kelvin wave (M1R1+) initial condition of amplitude $A_0 = -0.3$ is shown at several different times. Spectral resolution was chosen at $N = 70$ with time step $\Delta t = 0.0025$, although much larger time step is available. It should be noted here that since the model Eq. (40) is given in a "regularized" form (i.e. spatial derivative operators act on $\partial(U, V)^T/\partial t$, much larger time step can be allowed at the cost of solving the implicit Eq. (43) at every time step (e.g. see [5, pp. 181–182]). With the given spectral resolution the radial collocation is at $L = 108$ points, and the azimuthal collocation is at $K = 256$ points. Only a solution of the isopycnal surface Z is shown in the figure because it is the time integral of the divergence of the velocity field, containing important physical essence of the velocity field. Observing the figure, the negative side of the isopycnal surface travels faster than the positive side, generating a front that gradually steepens as it travels in the cyclonic (counter clockwise) direction (see Fig. 4(b) corresponding to $t = 8 \approx 1.4T$, where T is a linear wave period). The front continually steepens as the wave field evolves and it starts to generate a train of oscillatory waves (see Fig. 4(c) corresponding to $t = 16 \approx 2.7T$). The leading front passes eventually through its own oscillatory tail, generating ripples (see Fig. 4(d) corresponding to $t = 24 \approx 4.1T$), and the field becomes more complicated. The steepening of the wave-front is a familiar effect of nonlinearity, and subsequent generation of oscillatory waves results from an approximate balance between the nonlinearity and the dispersive effect in the model. This solution behavior is very similar to that found in the well known Korteweg de Vries equation, the fundamental model describing the weakly-nonlinear and the weakly-dispersive effect. The time integration consists of 28 000 time steps was performed stably.

Although not mentioned earlier, the resolution-doubling tests were conducted to examine the convergence of the numerical solutions. We emphasize here that such tests, although quite standard, are particularly useful in this case because the solutions in Fig. 4 exhibit the steep wave-front entailing sub-basin-scale, dispersive waves and even smaller waves, which
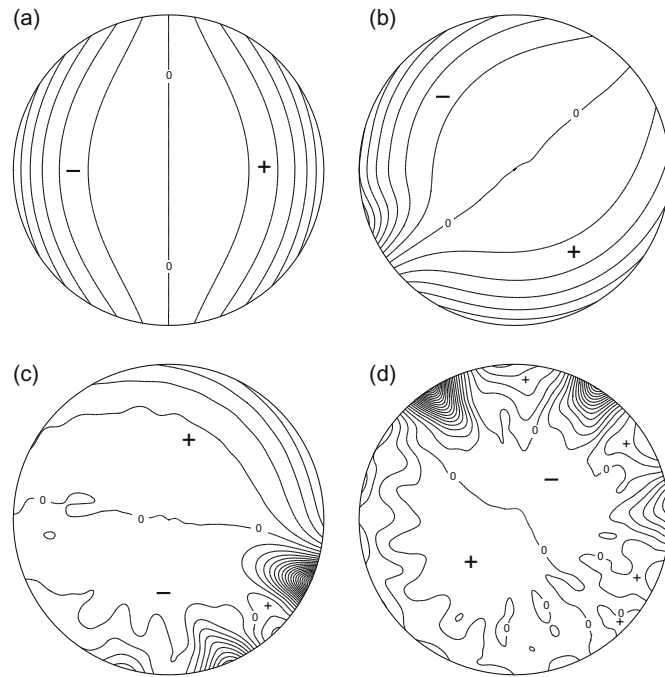
Fig. 4. Evolution of a Kelvin wave (M1R1+) initial condition of amplitude $A_0 = -0.3$ in the weakly-nonlinear and weakly-dispersive model. Snap shots of isopycnal surface Z are taken at (a) $t = 0$, (b) $t = 8$, (c) $t = 16$ and (d) $t = 24$. Contour level step is 0.05.
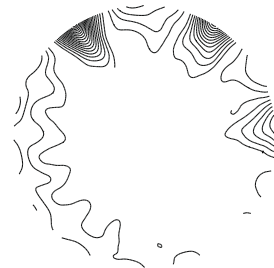

are always subject to a fundamental question whether they are physical (model-relevant) or just numerical artifacts related to under-resolution. In Fig. 5 solutions at different truncation levels are compared at the stage of the generation of dispersive waves after front steepening ($t = 16$) and subsequent generation of ripples ($t = 24$). A common time step $\Delta t = 0.0025$ was used for all the truncation levels. At $t = 16$ with the low truncation N23, small oscillations appear in the fore side of the cyclonically progressing front. Such oscillations are not physically relevant because the dispersion relation for the weakly-dispersive system does not allow high-wave-number waves to propagate faster than low-wave-number waves. These oscillations, which we refer to as Gibb's-type phenomena, are caused by an insufficient spectral resolution. It is clearly
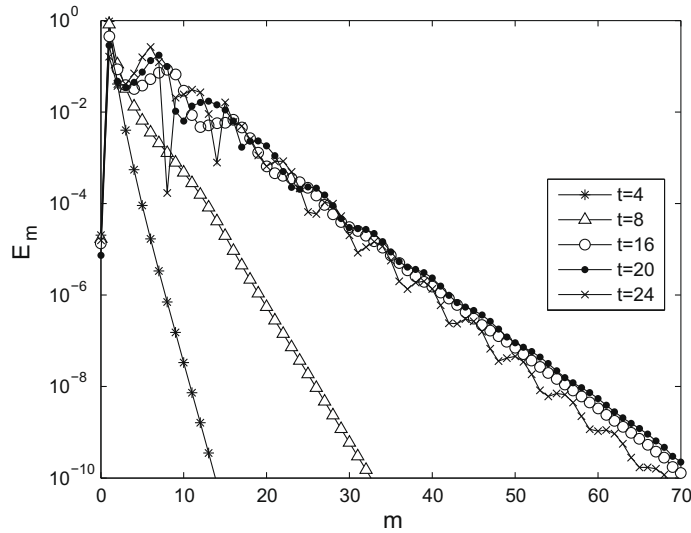
Fig. 6. Azimuthal modal energy spectrum at various time for the evolution field of the Kelvin wave initial condition (M1R1+).

observed from the figure that such Gibb's oscillations disappear for larger truncations. At $t = 24$ the dispersive waves are resolved to a certain level with N23, but it lacks ripples due to under-resolution as they are clearly observed in larger truncations. The solutions appear to be converged at N45 qualitatively, and further doubling the resolution to N90 yields almost indistinguishable results.

In Fig. 6 the total energy density (the integrand of the energy expression E in (37)) was calculated as a function of azimuthal mode m for several different times. Modal energies were all normalized by the total system energy. The spectral convergence is readily observed from the figure. Initially the energy is concentrated only in azimuthal mode $m = 1$. The initial energy is subsequently transferred to higher modes as the nonlinear wave-front steepens until the oscillatory waves are generated, and then the spectral convergence rate becomes almost saturated.
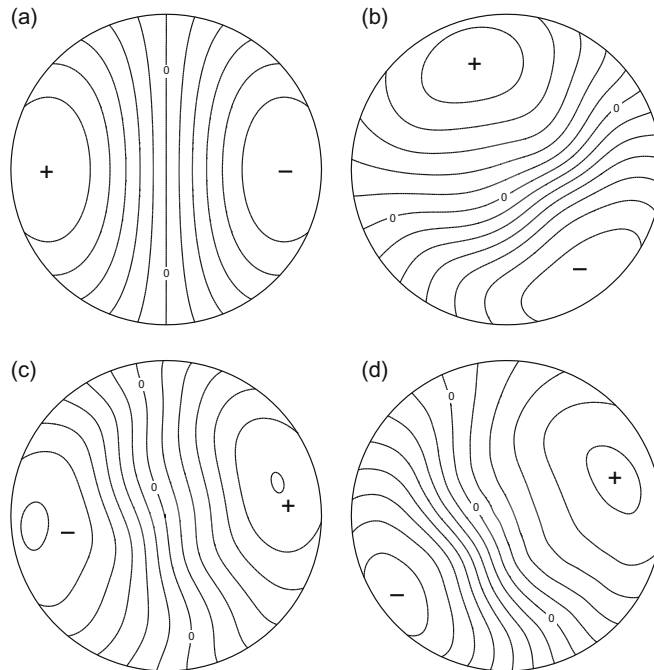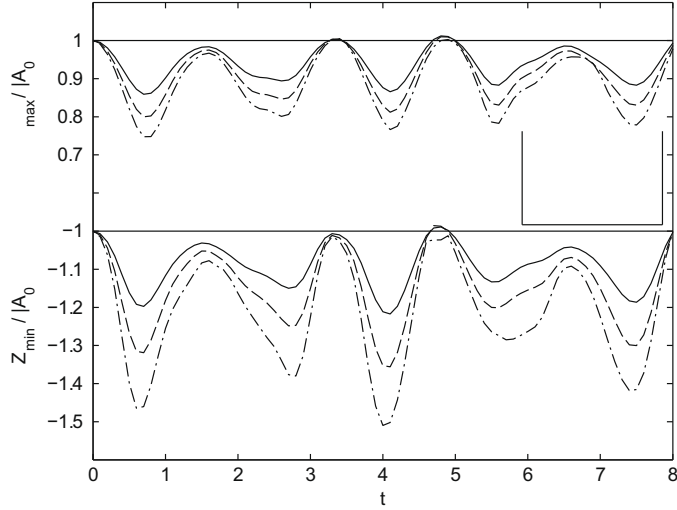

Fig. 7. Evolution of a Poincaré wave (M1R1−) initial condition of amplitude $A_0 = -0.3$ in the weakly-nonlinear and weakly-dispersive model. Snap shots of isopycnal surface Z are taken at (a) $t = 0$, (b) $t = 3$, (c) $t = 3.4$ and (d) $t = 24$. Contour level step is 0.05.

For the next example, an evolution of the Poincaré wave of azimuthal mode one and radial mode one (M1R1$-$) was examined and results are presented in Fig. 7. The numerical run configuration is the same as that in the Kelvin wave example described above. The initial condition is symmetric, but the field quickly loses its symmetry as it rotates in the anti-cyclonic (clockwise) direction (Fig. 7(b)). The evolving asymmetric field tends to return to a near symmetric field (Fig. 7(c)), and this repeats aperiodically for the rest of evolution. The numerical model was stably integrated, and it was run up to $t = 24$ which corresponds to about seventeen and half wave rotations around the center (Fig. 7(d)).

In Fig. 8 the maximum and minimum values of the isopycnal surface for different initial wave amplitudes A_0 are presented as a function of time. Values are normalized by the initial wave amplitude. The modulation of the amplitudes becomes larger as the initial amplitude increases, implying that the modulation is a nonlinear phenomenon. This pseudo recurrence of the Poincaré wave field has not been recognized before, but is clearly revealed by simulation employing the present numerical method.

5. Conclusions

In this paper we proposed a tau-method approach that can fully satisfy the regularity condition (kinematic constraint) and the boundary conditions of the solutions to vector field equations defined in the polar coordinates. This approach avoids an explicit coupling of radial basis functions of the polar vector field variables, and it enables one to utilize the original, simple form of the one-sided Jacobi polynomials as the radial basis if the vector field variables are transformed into the radial flux form. Also, the method provides flexibilities in specifying the boundary conditions without modification of the basis functions. Especially for the problem involving both vector and scalar functions, therefore, the implementation of the method is expected to be easier than that of the Galerkin method. The spectral convergence was demonstrated through the stable time integration of evolution equations comprising both the scalar and the vector fields. Since the tau-method seeks the solution to the modified equation, the conserved quantities of the original equation model are not generally conserved. But the variation of the quantity can be diminished to some negligible level with sufficient spectral and time resolutions.

The maximum allowable time step for hyperbolic-type equations is $O(N^{-2})$ for large truncations. For high-resolution, time-dependent problems, the Jacobi radial bases possibly lose their competitiveness in regard to computational efficiency over the Chebyshev polynomials. However, the proposed method with the Jacobi bases enforces all the regularity conditions at the origin and, therefore, one is able to obtain physically-behavioral, "worry-proof" solutions over the entire domain at all time levels of integration. This point is significantly important and should not be overlooked especially when one performs long-time integrations with hyperbolic-type equations. Because unphysical solution components (e.g. 2h-waves) related to insufficient treatment of regularity at the origin usually spread over the entire domain without being damped, polluting the entire solution field, the simulated field loses physical relevance. If there are nonlinear terms in the equations (as is usual in fluid mechanics), such numerical instabilities can be quite easily amplified by the nonlinear effects, rending the numerics quickly broken down.

In this paper we showed numerical examples only in a two-dimensional disc, but the proposed method can be readily extended to a three-dimensional, cylindrical domain (e.g. Navier–Stokes equations), and this area will be pursued in the future work.

Appendix A. Some properties of the Jacobi polynomials

We summarize some properties of the Jacobi polynomials referred in this paper. Although many useful properties are found in [23,17,9], care must be taken in the application because their definitions of the radial basis functions are slightly different. In this paper, we follow the definition established by Verkley [23].

The one-sided Jacobi polynomials are defined here as $Q_{mn}(r) = r^{|m|}P_k^{(\alpha,\beta)}(x)$ where $x = 2r^2 - 1$ and $n = |m| + 2k$. The arbitrary parameters (α, β) are kept as they are so as not to loose the generality.

A.1. Series expansions

Power series of the one-sided Jacobi polynomials is given by

$$Q_{mn}(r) = r^{|m|}P_k^{(\alpha,\beta)}(x) = (-1)^k \sum_{k'=0}^{k}(-1)^{k'} \frac{(\beta+1)_k(\beta+1+k+\alpha)_{k'}}{(\beta+1)_{k'}k'!(k-k')!}r^{|m|+2k'}. \tag{49}$$

From this expansion the coefficient of the leading power $r^{|m|}$ is used to obtain the kinematic constraint (18). The inverse expansion of (49) is also given by

$$r^{|m|+2k} = \sum_{k'=0}^{k} \frac{(2k'+\alpha+\beta+1)\Gamma(\beta+k+1)(k-k'+1)_{k'}}{(k+k'+\alpha+\beta+1)\Gamma(\beta+k'+1)(k'+\alpha+\beta+1)_k}Q_{mn'}(r). \tag{50}$$

The derivations of above expansions for a particular parameter set $(\alpha, \beta) = (0, |m|)$ are found in [23].

A.2. Formulae for derivatives

For calculation of the derivatives we employ a direct formula given by

$$\frac{d^l}{dx^l}P_k^{(\alpha,\beta)}(x) = \frac{(\alpha+\beta+k+1)_l}{2^l}P_{k-l}^{(\alpha+l,\beta+l)}(x). \tag{51}$$

Using this property the recurrence formula for the first derivative of $Q_{mn}(r)$ is expressed as

$$r\frac{dQ_{mn}(r)}{dr} = r^{|m|}\left\{|m|P_k^{(\alpha,\beta)}(x) + 2r^2(\alpha+\beta+k+1)P_{k-1}^{(\alpha+1,\beta+1)}(x)\right\}, \tag{52}$$

and the second derivative can be also expressed as

$$r^2\frac{d^2}{dr^2}Q_{mn}(r) = r^{|m|}\left\{|m|(|m|-1)P_k^{(\alpha,\beta)}(x) + 2(2|m|+1)(\alpha+\beta+k+1)r^2P_{k-1}^{(\alpha+1,\beta+1)}(x) + 4(\alpha+\beta+k+1)_2r^4P_{k-2}^{(\alpha+2,\beta+2)}(x)\right\}. \tag{53}$$

For $k \leqslant 1$ (alt. $|m| \leqslant n \leqslant |m|+2$), the derivatives are computed by the following:

$$r\frac{d}{dr}r^{|m|}P_0^{(\alpha,\beta)}(x) = |m|r^{|m|},$$
$$r^2\frac{d^2}{dr^2}r^{|m|}P_0^{(\alpha,\beta)}(x) = |m|(|m|-1)r^{|m|}, \tag{54}$$
$$r^2\frac{d^2}{dr^2}r^{|m|}P_1^{(\alpha,\beta)}(x) = \{-(|m|-1)_2(\beta+1) + (|m|+1)_2(\alpha+\beta+2)r^2\}r^{|m|}.$$

The derivatives (52) and (53) can be calculated by successively evaluating $P_k^{(\alpha,\beta)}(x)$ using the standard recurrence formula given by 22.7.1 in [1].

A.3. Boundary values

The standardization of the Jacobi polynomials is defined by 22.2.1 in [1] as

$$P_k^{(\alpha,\beta)}(1) = \binom{k+\alpha}{k} = \frac{(\alpha+1)_k}{k!}. \tag{55}$$

Hence, the boundary value of $Q_{mn}(r)$ at $r = 1$ is given by

$$Q_{mn}(1) = r^{|m|}P_k^{(\alpha,\beta)}(2r^2-1)\Big|_{r=1} = \frac{(\alpha+1)_k}{k!}. \tag{56}$$

The boundary value of the first derivative of $Q_{mn}(r)$ can be deduced using (55) and (52), given by the following

$$\frac{dQ_{mn}(r)}{dr}\Big|_{r=1} = \left\{|m| + \frac{2k(\alpha+\beta+k+1)}{\alpha+1}\right\}\frac{(\alpha+1)_k}{k!}. \tag{57}$$

This can be readily used to enforce Neumann boundary conditions.

Using a symmetry property $P_k^{(\alpha,\beta)}(-x) = (-1)^k P_k^{(\beta,\alpha)}(x)$ given by 22.4.1 in [1], $Q_{0n}(0)$ is obtained as

$$Q_{0n}(0) = P_k^{(\alpha,\beta)}(2r^2 - 1)\Big|_{r=0} = P_k^{(\alpha,\beta)}(-1) = (-1)^k P_k^{(\beta,\alpha)}(1) = (-1)^k \frac{(\beta+1)_k}{k!}, \tag{58}$$

where (55) is used in the last step. This property is used to construct the radial expansion function of the radial velocity flux given by (14). Accordingly, the Dirichlet boundary condition of the radial velocity flux (19) is obtained using the property (56).

Appendix B. Derivation of expansion coefficients

We describe the derivation of the expansion coefficients of the exact solution to the linear evolution model given in (35). Here we consider expanding the non-scaled radial function of radial velocity flux $\tilde{U}_m^*(r)$ in terms of the one-sided Jacobi polynomials with parameter set $(\alpha, \beta) = (0, m)$, that is $Q_{mn} = r^m P_k^{(0,m)}(2r^2 - 1)$ assuming $m > 0$. Taking the Poincaré wave mode $J_m(\lambda r)$ for $Z_m(r)$ in (32), and using the recurrence relation $J_m'(x) = J_{m-1}(x) - mJ_m(x)/x$, $\tilde{U}_m^*(r)$ is written

$$\tilde{U}_m^*(r) = (1 + \omega)mJ_m(\lambda r) - \lambda\omega rJ_{m-1}(\lambda r). \tag{59}$$

Expansion of $J_m(\lambda r)$ in terms of $Q_{mn}(r)$ is already derived by Verkley [24] as following

$$J_m(\lambda r) = \frac{2}{\lambda} \sum_{k=0}^{\infty} (-1)^k (n+1) J_{n+1}(\lambda) Q_{mn}(r), \quad \text{and } n = m + 2k. \tag{60}$$

The term $rJ_{m-1}(\lambda r)$ in (59) can be expanded in terms of $Q_{mn}(r)$ by following the similar procedure to derive above expansion described in [24]. Using the power series expansion of the Bessel function, $rJ_{m-1}(\lambda r)$ is written

$$rJ_{m-1}(\lambda r) = \left(\frac{\lambda}{2}\right)^{m-1} \sum_{k=0}^{\infty} \frac{(-1)^k}{k!(m-1+k)!} \left(\frac{\lambda}{2}\right)^{2k} r^{m+2k}. \tag{61}$$

Expansion of polynomial power r^{m+2k} in terms of $Q_{mn}(r)$ is given by (50) in Appendix A with $(\alpha, \beta) = (0, m)$

$$r^{m+2k} = r^n = \sum_{k'=0}^{k} \frac{(m+2+2k')(k-k'+1)_{k'}}{(m+2+k+k')(m+2+k)_{k'}} Q_{mn'}(r). \tag{62}$$

Substituting (62) into (61), and converting terms with Pochhammer symbol to the factorial form, we get

$$rJ_{m-1}(\lambda r) = \left(\frac{\lambda}{2}\right)^{m-1} \sum_{k=0}^{\infty} \sum_{k'=0}^{k} \frac{(-1)^k(m+k)(m+1+2k')}{(k-k')!(m+1+k+k')!} \left(\frac{\lambda}{2}\right)^{2k} Q_{mn'}(r). \tag{63}$$

Changing the order of summations we write this expression as

$$rJ_{m-1}(\lambda r) = \sum_{k'=0}^{\infty} (m+1+2k') Q_{mn'}(r) \left\{ \left(\frac{\lambda}{2}\right)^{m-1} \sum_{k=k'}^{\infty} \frac{(-1)^k(m+k)}{(k-k')!(m+1+k+k')!} \left(\frac{\lambda}{2}\right)^{2k} \right\}. \tag{64}$$

The bracketed sum $\{\cdots\}$ is decomposed into two sums

$$\{\cdots\} = \left(\frac{\lambda}{2}\right)^{m-1} \sum_{k=k'}^{\infty} \frac{(-1)^k}{(k-k')!(m+k+k')!} \left(\frac{\lambda}{2}\right)^{2k} - (k'+1)\left(\frac{\lambda}{2}\right)^{m-1} \sum_{k=k'}^{\infty} \frac{(-1)^k}{(k-k')!(m+1+k+k')!} \left(\frac{\lambda}{2}\right)^{2k}. \tag{65}$$

Letting $k - k' = l$, this is written in a following form

$$\{\cdots\} = (-1)^{k'}\left(\frac{2}{\lambda}\right)\left[\left(\frac{\lambda}{2}\right)^{m+2k'} \sum_{l=0}^{\infty} \frac{(-1)^l}{l!(m+2k'+l)!} \left(\frac{\lambda}{2}\right)^{2l}\right] - (-1)^{k'}(k'+1)\left(\frac{2}{\lambda}\right)^2\left[\left(\frac{\lambda}{2}\right)^{m+1+2k'} \sum_{l=0}^{\infty} \frac{(-1)^l}{l!(m+1+2k'+l)!} \left(\frac{\lambda}{2}\right)^{2l}\right]. \tag{66}$$

Recalling the series expansion of the Bessel function, the first square bracketed term is $J_{m+2k'}(\lambda)$, and the second bracketed one is $J_{m+2k'+1}(\lambda)$. Writing the expression explicitly, we have that

$$\{\cdots\} = (-1)^{k'}\left(\frac{2}{\lambda}\right)J_{m+2k'}(\lambda) - (-1)^{k'}(k'+1)\left(\frac{2}{\lambda}\right)^2 J_{m+2k'+1}(\lambda). \tag{67}$$

Substituting (67) into (64) and using $m + 2k' = n'$, $rJ_{m-1}(\lambda r)$ is expanded in the form

$$rJ_{m-1}(\lambda r) = \frac{2}{\lambda} \sum_{k'=0}^{\infty} (-1)^{k'}(n'+1)\left\{ J_{n'}(\lambda) - \frac{2}{\lambda}(k'+1)J_{n'+1}(\lambda) \right\} Q_{mn'}(r). \tag{68}$$

Substituting (68) and (60) into (59), we obtain the expansion coefficients of $\widetilde{U}_m^*(r)$ given in (35). The expansion of $\widetilde{V}_m^*(r)$ is obtained through a procedure similar to that described above. Corresponding expansion coefficients for the Kelvin wave mode $I_m(\lambda r)$ are easily deduced by replacing λ with $i\lambda$, and using the identity $J_n(ix) = (i)^n I_n(x)$ in (35). It turns out that the J-Bessel functions are replaced with I-Bessel functions, and alternating signs $(-1)^k$ are eliminated in (35).

References

[1] M. Abramowitz, I.A. Stegun, Handbook of Mathematical Functions, Dover, 1972.
[2] F. Auteri, L. Quartapelle, Spectral solvers for spherical elliptic problems, J. Comput. Phys. 227 (2007) 36–54.
[3] F. Auteri, L. Quartapelle, Spectral elliptic solvers in a finite cylinder, Commun. Comput. Phys. 5 (2009) 426–441.
[4] M. Born, E. Wolf, Principles of Optics, seventh ed., Cambridge University, 1999.
[5] J.P. Boyd, Chebyshev and Fourier Spectral Methods, second ed., Dover, 2001.
[6] G.T. Csanady, Large-scale motion in the great lakes, J. Geophys. Res. 72 (16) (1967) 4151–4162.
[7] H. Eisen, W. Heinrichs, K. Witsch, Spectral collocation methods and polar coordinate singularities, J. Comput. Phys. 96 (1991) 241–257.
[8] D. Gottlieb, S. Orszag, Numerical analysis of spectral methods; theory and applications, CBMS-NSF Regional Conference Series in Applied Mathematics. SIAM, Philadelphia, PA, 1977.
[9] K. Ishioka, Spectral model for shallow-water equation on a disk. I: Basic formulation, J. Jpn. Soc. Fluid Mech. 22 (2003) 345–358.
[10] K. Ishioka, Spectral model for shallow-water equation on a disk. II: Numerical examples, J. Jpn. Soc. Fluid Mech. 22 (2003) 429–441.
[11] V.I. Krylov, Approximated Calculation of Integrals, Dover, 2006.
[12] Sir H. Lamb, Hydrodynamics, sixth ed., Dover, 1932.
[13] A. Leonard, A. Wray, A new numerical method for the simulation of three-dimensional flow in a pipe, in: E. Krause (Ed.), Proceedings of the Eighth International Conference on Numerical Methods in Fluid Dynamics, Aachen, Germany, Springer-Verlag, Berlin, June 28–July 2, 1982.
[14] H.R. Lewis, P.M. Bellan, Physical constraints on the coefficients of fourier expansions in cylindrical coordinates, J. Math. Phys. 31 (11) (1990) 2592–2596.
[15] P.W. Livermore, C.A. Jones, S.J. Worland, Spectral radial basis functions for full sphere computations, J. Comput. Phys. 227 (2007) 1209–1224.
[16] J.M. Lopez, F. Marques, Jie Shen, An efficient spectral-projection method for the Navier–Stokes equations in cylindrical geometries. II: Three-dimensional cases, J. Comput. Phys. 176 (2002) 384–401.
[17] T. Matsushima, P.S. Marcus, A spectral method for polar coordinates, J. Comput. Phys. 120 (1995) 365–374.
[18] P.E. Merilees, An alternative scheme for a summation of a series of spherical harmonics, J. Appl. Meteor. 12 (1973) 224–227.
[19] R.J. Noll, Zernike polynomials and atmospheric turbulence, J. Opt. Soc. Am. 66 (1976) 207–211.
[20] S.A. Orszag, Fourier series on spheres, Mon. Weather Rev. 102 (1974) 56–75.
[21] S.A. Orszag, A.T. Patera, Secondary instability of wall-bounded shear flows, J. Fluid Mech. 128 (1983) 347–385.
[22] V.G. Priymak, T. Miyazaki, Accurate Navier–Stokes investigation of transitional and turbulent flows in circular pipe, J. Comput. Phys. 142 (1998) 370–411.
[23] W.T.M. Verkley, A spectral model for two-dimensional incompressible fluid flow in a circular basin. I: Mathematical foundation, J. Comput. Phys. 136 (1997) 100–114.
[24] W.T.M. Verkley, A spectral model for two-dimensional incompressible fluid flow in a circular basin. II: Numerical examples, J. Comput. Phys. 136 (1997) 115–131.
[25] von F. Zernike, Beugungstheorie des schneidenverfahrens und seiner verbesserten form, der phasenkontrastmethode, Physica 1 (1934) 689–704.